CrossMark

Increase of antimicrobial and photocatalytic properties of silver-doped PbS obtained by sonochemical method

N. F. Andrade Neto[1] · Y. G. Oliveira[1] · C. A. Paskocimas[1] · M. R. D. Bomio[1] · F. V. Motta[1]

Abstract

In this work, pure PbS powders doped with silver were obtained in the proportions of 1, 2, 4 and 8 mol% by sonochemical method. Powders were characterized by X-ray diffraction (XRD), field emission scanning electron microscopy (FE-SEM), UV–Vis spectroscopy (UV–Vis) and EPR analysis. The photocatalytic properties were estimated by degradation of methylene blue dye. The antimicrobial properties were studied by the formation of inhibition halos against *Escherichia coli* and *Staphylococcus aureus* bacteria and *Candida albicans* yeast. XRD patterns show that PbS, with a cubic structure, was obtained without the formation of secondary phases. FE-SEM analysis indicates loss of the cubic aspect of PbS samples as the Ag^+ concentration increases and particle size reduces. The defects generated by the substitution of Pb^{2+} by Ag^+ increase the photocatalytic activity, where PbS and P8A samples reduced by 25% and 68%, respectively, the MB concentration and significantly increased the antimicrobial activity against *E. coli* and *S. aureus* bacteria and *C. albicans* yeast.

1 Introduction

Population increase leads to greater industrial production and, consequently, greater waste generation [1, 2]. Waste from textile industries are difficult to be processed using conventional methods due to the presence of –N=N– groups linked to aromatic rings, requiring specific methods for their processing [3]. Therefore, it is necessary to use less conventional methods, such as heterogeneous photocatalysis [4, 5]. Heterogeneous photocatalysis is characterized by the use of semiconductor to generate electron/hole (e^-/h^+) pairs that mineralize the organic molecules of dyes [6, 7]. Reactive oxygen species (ROS) generated by e^-/h^+ pairs also have antimicrobial action, enabling semiconductor materials to be used in the treatment of microorganisms resistant to antibiotic treatments [8, 9].

Semiconductor materials have been widely studied due to their high optical and electronic properties [10]. Moreover,

their properties can be easily altered by the manipulation of defects in their crystalline lattice [11, 12]. Several semiconductor materials such as TiO_2 [13], AgCl [14], SnO_2 [15], ZnO [16], and others, have been widely studied. Lead-based materials have gained attention due to their range of possibilities and applications, such as supercapacitors [17], photocatalytic activity [18], lithium storage [19], electrodes [20], and others. Among lead-based materials, PbS is an important semiconductor of the IV-VI group, which has excellent optical and optoelectronic properties [21].

However, to use PbS in photovoltaic, photocatalytic, photodetection and antimicrobial applications, it is crucial to improve its separation efficiency of photogenerated electrons and holes, which can be achieved through doping [22]. Silver is an attractive noble metal with high electrical conductivity to facilitate fast electron transfer [23]. Hu et al. [24] obtained significant improvements in the performance and stability of solar cells based on PbS films by the addition of silver, where carrier concentration and mobility and the extreme band, as well as Fermi energy levels, can be adapted by adjusting the Ag/Pb ratio.

In this work, silver-doped PbS powders (PbS:xAg with x = 0, 1, 2, 4 and 8 mol%) were obtained by the sonochemical method. Powders were characterized by X-ray diffraction (XRD), Fourier transform infrared spectroscopy (FTIR), field emission scanning electron microscopy (FE-SEM) and diffuse reflectance spectroscopy. The photocatalytic activity

✉ N. F. Andrade Neto
nfandraden@gmail.com

1 LSQM, DEMAT, UFRN, Av. Sen. Salgado Filho, 3000, CEP 59072-970 Natal, RN, Brazil

was measured with methylene blue dye when submitted to UV radiation. The antimicrobial activity was estimated against *S. aureus* and *E. coli* bacteria and *C. albicans* yeast.

2 Materials and methods

PbS powders were obtained by the sonochemical method, using lead nitrate ($Pb(NO_3)_2$, Sigma–Aldrich, 99%), thiourea (H_2NCSNH_2, Synth, 99%), silver nitrate ($AgNO_3$, Strem Chemicals, 99.9%), sodium hydroxide (NaOH, Synth, 98%) and deionized water as received.

Initially, lead nitrate and thiourea were weighed, maintaining the molar ratio of 1:1 (1.383 g/0.315 g), and kept under constant stirring in 50 mL of deionized water. After solution homogenization, sodium hydroxide (approximately 1 g) was added to control pH, fixing it at 12, keeping under stirring. The solution was then taken to Branson 102C ultrasonic tip, operating at 20 kHz frequency, for 30 min. The solution was then washed and centrifuged to obtain the powder (PbS), which was oven dried for 24 h. Ag^+ doped samples were obtained in a similar way, always respecting the ratio of 1, 2, 4 and 8 mol% in relation to lead. Samples were named P1A, P2A, P4A and P8A, according to the molar Ag^+ percentage added.

The phases obtained for pure and Ag-doped PbS powders were investigated using the Shimadzu diffractometer (XRD-6000) with CuKα radiation (1.5418 Å). In order to better verify the changes promoted by doping, refinement was performed using the General Structure Analysis System (GSAS) software with graphic interface EXPGUI [25]. Field emission scanning electron microscopy (FE-SEM) was used to observe the morphology. Elemental X-ray fluorescence analysis (XRF) was performed on the Shimadzu EDX-720 spectrometer to analyze the silver doping efficiency in PbS.

UV–Vis spectroscopy was performed on Shimadzu (UV-2550) equipment, with wavelength range of 200–900 nm and programmed for the diffuse reflectance mode, and based on these results, the optical gap band (Egap) energy of these materials was determined using the Wood and Tauc Equation [26]. The sample was placed in a quartz tube for the EPR measurements. The analysis occurred in room temperature using the EMM micro-9.5/12/S/W spectrometer, operated in 9.833 GHz frequency and 25 dB alternation.

The photocatalytic properties of powders were tested against methylene blue (MB) dye of molecular formula [$C_{16}H_{18}ClN_3S$] (Mallinckrodt, with 99.5% purity), under UV–Vis radiation. About 0.05 g of powder were placed in beaker containing 50 mL of MB (1×10^{-5} mol/L^{-1}) and kept under constant stirring, illuminated by six UVC lamps (TUV Philips, 15W, with maximum intensity of 254 nm = 4.9 eV). At intervals of 30 min, 2 mL aliquot was collected and the absorbance spectrum variation was analyzed using

Shimadzu spectrometer (model UV-2600). By these values, the dye concentration variation was determined by the test time.

The antimicrobial properties of powders were evaluated by in vitro tests using agar diffusion method against gram negative *E. coli* (ATCC-25922) and gram positive *S. aureus* bacteria (ATCC-25923) and *C. albicans* yeast (CA14), according to standard procedures stipulated by the Institute of Clinical and Laboratory Standards (CLSI), similarly to study carried out by Araújo et al. [27]. The inoculum was prepared by direct suspension of colonies in phosphate-buffered saline (PBS) in water plate and maintained for 24 h at 35 °C. The solution turbidity was then adjusted according to the McFarland scale (bacterial density of 1×10^8 CFU/mL). The test was performed using the well diffusion technique with 6 mm wells and adding 50 μL sample aliquots.

3 Results and discussion

Figure 1 shows the XRD patterns of pure and silver-doped PbS samples. The patterns indicate the formation of PbS, with cubic crystalline system and Fm-3m space group (no. 225), characterized by JCPDS card 65-2935. The characteristic PbS peaks in 2θ = 26.02, 30.06, 43.14 and 51.13° refer to (111), (200), (220) and (311) planes, respectively. The presence of defined peaks and with considerable intensity indicates the high crystallinity of pure PbS samples. Tshemese et al. [28] observed, by increasing the intensity of XRD patterns, the increase in the crystallinity of PbS nanoparticles by raising the synthesis temperature from 150 to 200 °C. The reduction in the intensity of characteristic peaks with the increase in the amount of dopant occurs due to defects generated in the crystalline lattice as a result of differences
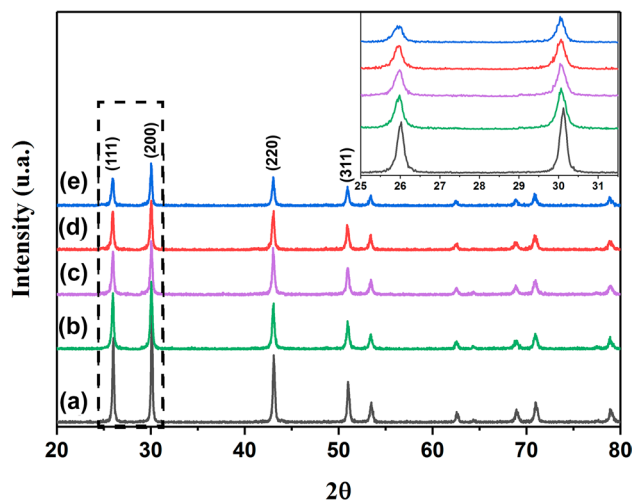

Fig. 1 XRD patterns for (a) PbS, (b) P1A, (c) P2A, (d) P4A and (e) P8A samples

between ionic rays and the valence of Pb^{2+} (1.19 Å) and Ag^+ ions (1.15 Å). El-kemary et al. [29] observed that the addition of Ag^+ in the crystalline lattice of CdO generates a reduction in the intensity of diffraction peaks due to the generation of defects. The reduction in the intensity of characteristic PbS peaks and the non-appearance of the secondary phase indicate that the sonochemical method is efficient in obtaining silver-doped PbS.

For analysis of possible differences in structural arrangements induced by the addition of Ag^+ in the PbS lattice, the Rietveld refinement was used [30]. The General Structure Analysis System (GSAS) software with EXPGUI graphic interface was used to perform the refinement [25]. JCPDS card 65-2935 was used for refinement. The parameters used in refining were: scale factor and phase fraction; background, which was modeled using a displaced Chebyshev polynomial function; peak shape, which was modeled using Thomson-Cox-Hasting pseudo-Voigt; change in lattice constants; fractional atomic coordinates; and isotropic thermal parameters. The Rietveld refinement results are shown in Fig. 2 and Table 1.

By the small difference obtained between observed (obs) and theoretically calculated (calc) curves, it was concluded that the diffractogram patterns of samples are well adapted to the JCPDS card 65-2935. In addition, the χ^2, R_{wp} and R_p reliability parameters exhibit low values, indicating good

Table 1 Structural parameters of the Rietveld refinement for pure and silver-doped PbS samples

Sample	PbS	P1A	P2A	P4A	P8A
a (Å)	5.9408	5.9406	5.9401	5.9390	5.9366
Cell volume (Å^3)	209.669	209.648	209.595	209.478	209.225
Crystallite size (nm)	46.92	29.58	27.47	26.17	25.12
Microstrain (x 10^4)	9.010	1.611	2.316	5.585	2.423
χ^2	1.063	1.097	1.036	1.275	1.376
R_{wp}	0.2965	0.3304	0.3605	0.3351	0.3567
R_p	0.2221	0.2513	0.2965	0.2413	0.2879
Occ					
Pb^{2+}	1.0	0.9858	0.9781	0.9601	0.9106
Ag^+	0.0	0.0142	0.0219	0.0399	0.0894

quality of structural refinements and numerical results. These results confirm that samples are isostructural and crystals are well adapted to the cubic structure and Fm-3m spatial group (No. 225). The values obtained from the occupation of Pb^{2+} and Ag^+ cations in the unit cell are close to the synthesis stoichiometric values, confirming that doping was successfully performed.

Through the results shown in Table 1, the volume of unit cells is reduced with the addition of Ag^+. This occurs due
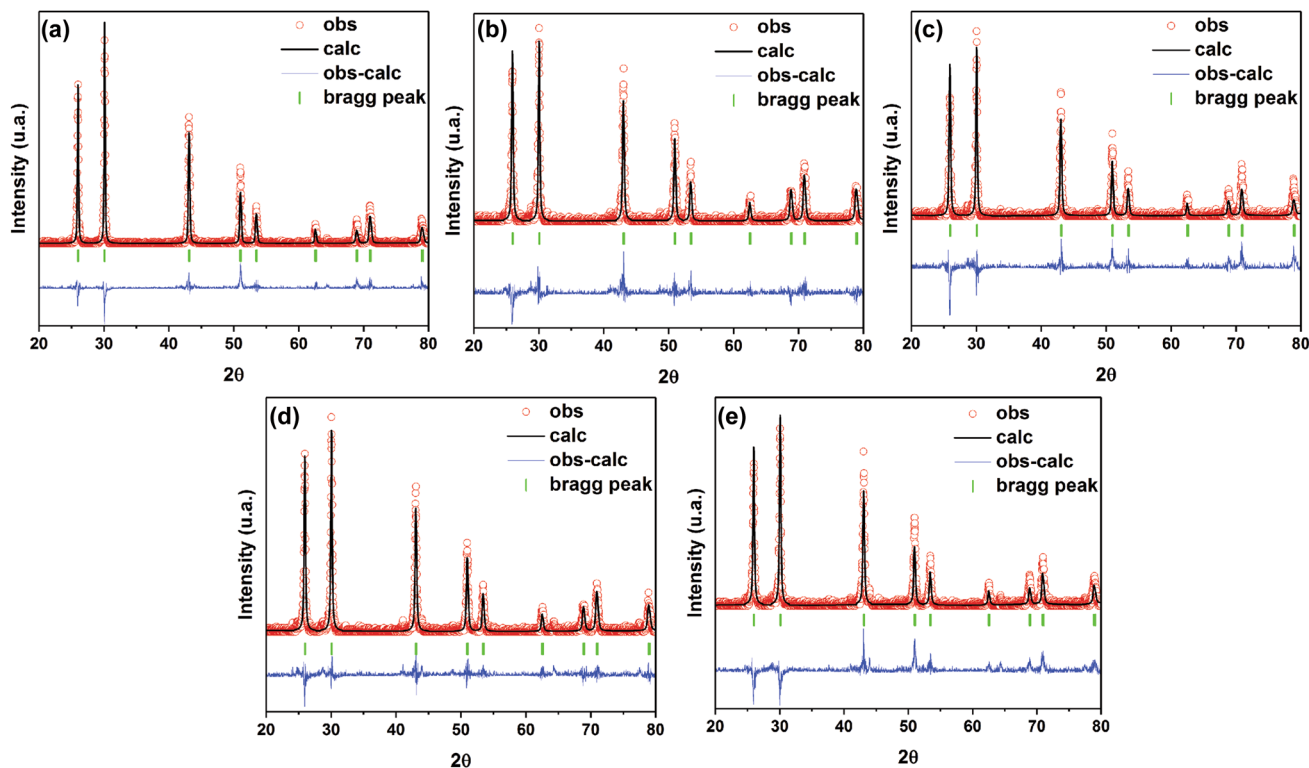

Fig. 2 Rietveld refinement for **a** PbS, **b** P1A, **c** P2A, **d** P4A and **e** P8A samples

to the substitution of Pb^{2+} cations for Ag^{+}, which have ionic radius of 1.19 Å and 1.15 Å, respectively. The increase in the amount of dopant causes more defects in the crystal lattice of PbS, yielding smaller crystallite sizes. This behavior is in accordance with Vergard's law, where for solid metal solutions, the unit cell dimensions tend to decrease with increasing dopant concentration [31, 32].

There were no changes in the x, y and z positions occupied by Pb^{2+}/Ag^{+} cations in the unit cell, being x, y and z = 0.50. S^{2-} anions maintained their positions in the x, y and z axes, which value is 0.00. The cubic crystalline structure of PbS is formed by Pb^{2+}/Ag^{+} cations arranged in the centered cube surrounded by six S^{2-} anions. Figure 3 shows the unit cells of samples obtained from the Rietveld refinement data.

Figure 4 shows the FE-SEM images obtained for pure and silver-doped PbS samples. Figure 4 shows that pure and silver-doped PbS particles are agglomerated and tend to form a rectangular morphology, with a non-uniform size distribution. As the silver concentration increases (Fig. 4a–e), a gradual reduction in particle size occurs, in addition to the appearance of nanoparticles with semi-spherical morphology, as can be seen in Fig. 4e. The reduction in mean particle size is in accordance with Fig. 1, where, as the silver concentration increases, the width of characteristic peaks also increases, indicating smaller crystallite size, which is usually accompanied by a reduction in particle size [33].

This relationship between width of diffraction peaks and PbS particle size was also observed in the study of Tshemese et al. [28].

The real reason for particle agglomeration is difficult to explain, mainly because nanometer-scale particles have high surface energy. The Ostwald ripening growth mechanism can be considered the most appropriate because it relates the critical core size and the surface energy of the particle without excess surfactant [34, 35]. This mechanism shows that even when several nanoparticles arise simultaneously, over time, larger particles tend to consume smaller ones to reduce their surface energy [35]. The use of surfactants during synthesis promotes alteration in the surface energy of particles, being able to avoid their agglomeration and alter their morphology [36]. However, morphological alteration resulting from the use of surfactants may be detrimental to the surface area dependent properties of materials, where a morphological alteration may promote the increase of its surface area and, consequently, a reduction of the reactive area of particles. Dong et al. [37] observed that the use of different anionic, cationic and non-ionic surfactants generated an increase in the surface area of CuO particles when compared to particles obtained without surfactant.

Figure 5 shows the XRF spectra obtained for the PbS and PA1 samples. All measurements were performed under vacuum atmosphere. Figure 5a shows the appearance of the peaks referring to Pb and S. As the analysis
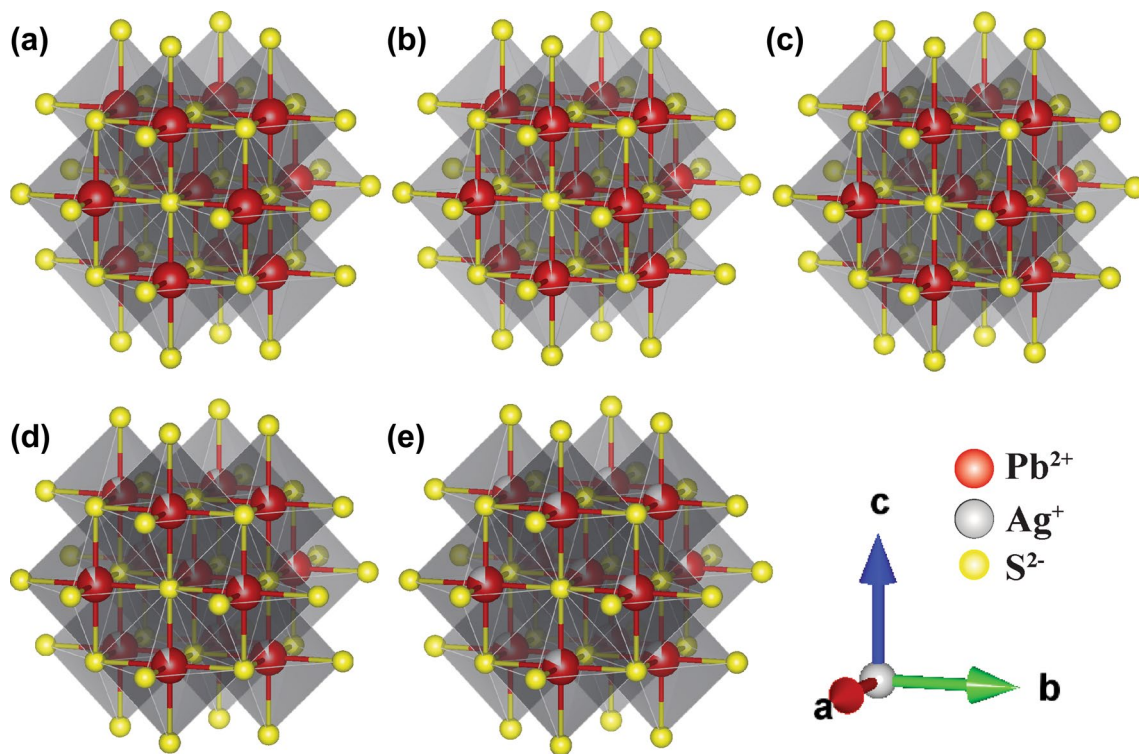

Fig. 3 Model of hexagonal structure for **a** PbS, **b** P1A, **c** P2A, **d** P4A and **e** P8A samples
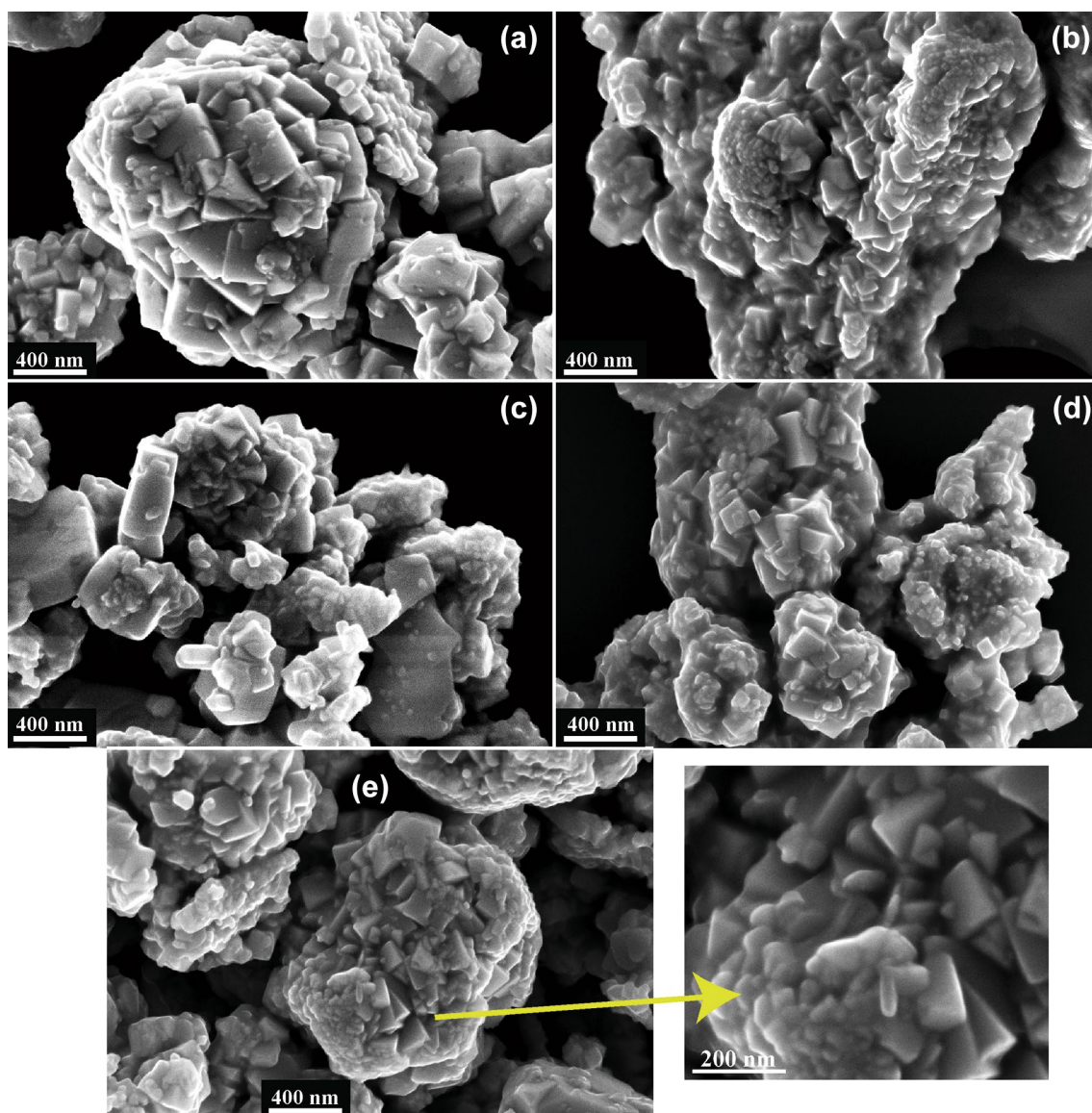
Fig. 4 Micrographs obtained by FE-SEM for **a** PbS, **b** P1A, **c** P2A, **d** P4A and **e** P8A samples

was performed from 0 to 25 keV, the formation of the peak referring to the Pb-Kα transition was not noticed, the Lα, Lβ and Lγ transitions appear in 10.552, 12.614 and 14.765 keV, respectively. There is an overlap in S-kα and S-kβ transitions, due to the energetic proximity (2.308 and 2.464 keV, respectively). According to Fig. 5b, the occurrence of the silver transition characteristic kα, at approximately 22.105 keV, confirming that doping occurred.

The diffuse reflectance spectroscopy technique in the visible ultraviolet region was used to estimate the gap band (Egap) of pure and doped PbS powders. The Kubelka–Munk function [38] was used to convert reflectance data into absorbance. The Wood and Tauc method [26] was used to estimate the optical gap band value (E_{gap}).

In the Wood and Tauc method, the optical gap energy is given by:

$$F(R)h\nu \propto \left(h\nu - E_{gap}\right)^{K} \tag{1}$$

Where: h is the Planck constant, v is the frequency, F(R) is the absorbance and k is indicated for different transitions (k = 1/2, 2, 3/2 or 3 for permissible direct, permissible indirect, direct prohibited and indirect prohibited, respectively). For pure and silver-doped PbS powders, k = ½ was admitted, that is, permissible direct. The absorbance *versus* photon energy values (eV) were plotted, extrapolating the linear portion of the curve to zero absorption to estimate Egap. Figure 6 shows the graph obtained by extrapolating
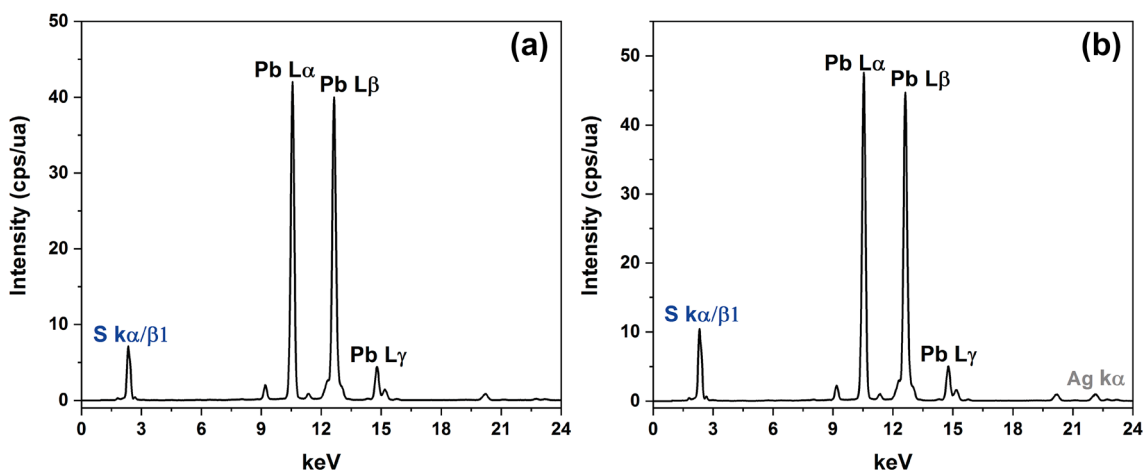
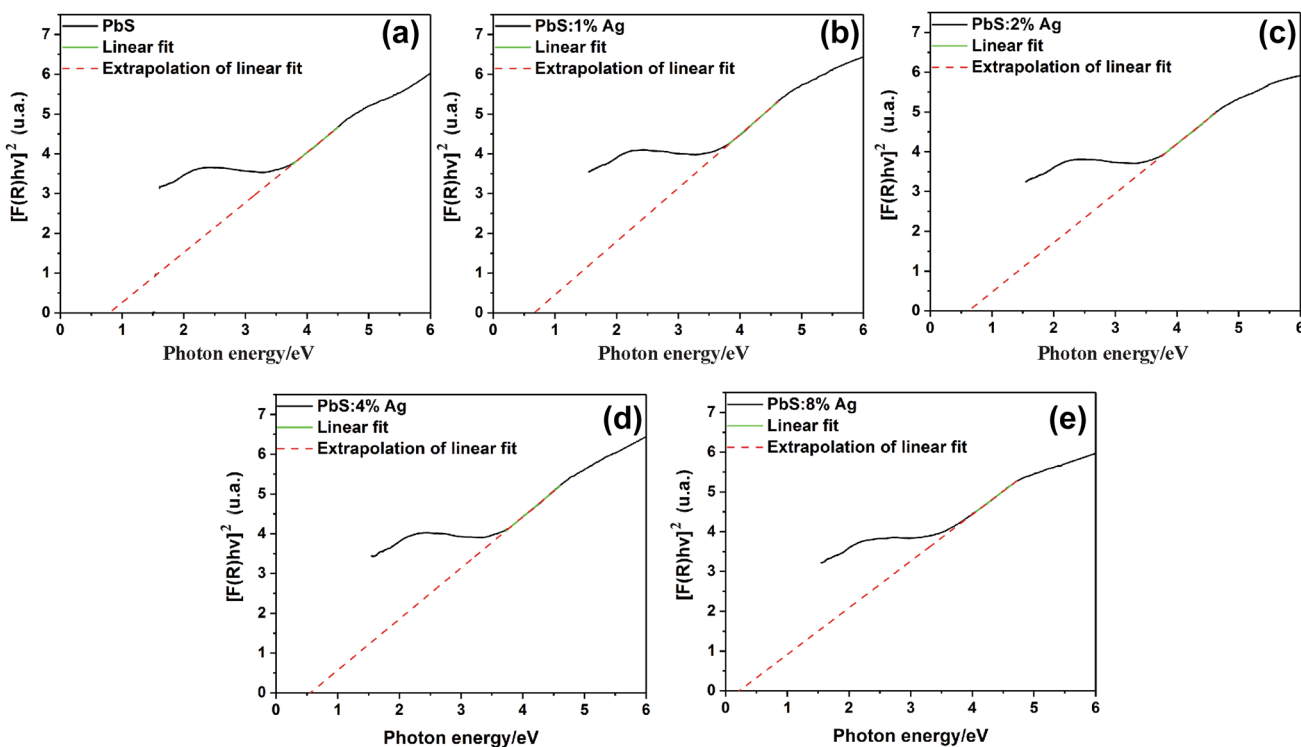**Fig. 5** XRF spectra for the **a** PbS and **b** P1A samples

Fig. 6 Extrapolation of UV–Visible Absorbance Spectrum for direct E_{gap} estimation for **a** PbS, **b** P1A, **c** P2A, **d** P4A and **e** P8A

Table 2 Direct Egap values obtained by extrapolating the linear portion of the absorbance spectrum

Sample	PbS	P1A	P2A	P4A	P8A
Direct Egap (eV)	0.79	0.66	0.62	0.55	0.23

the UV–Visible absorption spectrum to obtain direct Egap. Table 2 shows the direct Egap values for all samples.

Through values shown in Table 2, it could be observed that PbS has a direct Egap of 0.79 eV, such values are in accordance with values found in literature [39, 40]. According to Table 2, the increase in the amount of Ag^+ generates a gradual reduction in the direct Egap values. The reduction of Egap values is related to the increase in the structural disorder of PbS due to differences in ionic radius (1.19 Å e

1.15 Å) and valence between Pb^{2+} and Ag^+, the latter being the most effective. The difference between valences of cations generates an increase in the number of anion vacancies, generating intermediate levels between valence and conduction bands, reducing the Egap value of the material [41]. Ali et al. [42] observed that the addition of silver atoms in TiO_2 lattice generates, in addition to structural disorder, a displacement of the absorption band to the red region, resulting in lower Egap.

The photocatalytic activity of pure and silver-doped PbS samples was estimated against methylene blue dye (MB), under UV irradiation, with total test time of 180 min, and an aliquot was collected every 30 min. Figure 7a shows the variation of methylene blue concentration by the test time. The photocatalytic process may be described by a first-order kinetic model with relation to the absorbance of methylene blue [43], and the results obtained are shown in Fig. 7b. The graph shows the linear relationship of ln (C/Co) by the irradiation time. From this linear relationship, Eq. 2 was use and the kinetic constant (K) and the correlation coefficient (R^2) were obtained, which are shown in Table 3.

$$\frac{-\ln ct}{Co} = k \cdot t \tag{2}$$

where Ct is absorbance of methylene blue at time t; Co is initial absorbance; t is irradiation time; k is kinetic constant.

Through the results obtained from varying the MB concentration over time (Fig. 7a), pure PbS reduces approximately 25% the methylene blue concentration after 180 min. As the Ag^+ concentration increases in the PbS lattice, an increase in the photocatalytic activity is observed, where, for P8A sample, the MB concentration was reduced by approximately 68% after 180 min. The increase in photocatalytic activity can be accompanied by the constant K values shown

Table 3 Apparent first-order rate constant K of photocatalytic degradation and correlation coefficient R^2

Sample	$K \times 10^{-3}$ (min^{-1})	R^2
PbS	1.69	0.9553
P1A	2.53	0.9690
P2A	4.89	0.9403
P4A	6.05	0.9662
P8A	7.57	0.9648

in Table 3. The kinetic constant relates the efficiency of the semiconductor in the degradation of the dye and was used for a better monitoring of the photocatalytic behavior during the course of the test, accompanied by the adjustment R^2. Higher K values indicate that photocatalysis is more efficient. The photocatalytic activity of semiconductor materials is directly related to the impedance of the electron/hole pair recombination (e^-/h^+), because they act in the generation of hydroxyl radicals ($OH^\bullet$), which are strong oxidizing agents of organic materials, as dyes [44, 45]. Higher amounts of dopant present the best photocatalytic activities because they generate more anion vacancies, which act to prevent the recombination of e^-/h^+ pairs [44, 46]. As previously described, Ali et al. [42] showed that the addition of silver atoms in the TiO_2 lattice displaces the absorption band towards the red region, such a function acts in order to prevent the recombination of e^-/h^+ pairs, increasing the photocatalytic activity of the material.

Figure 8 shows the EPR spectra obtained for samples of pure PbS and doped with 1 and 8%Ag. The signals were obtained with the presence of a standard band, referring to the sample port, characterized by the letter a. The appearance of the band b is related to the Ag^0 ion ($4d^{10}5s^1$). The
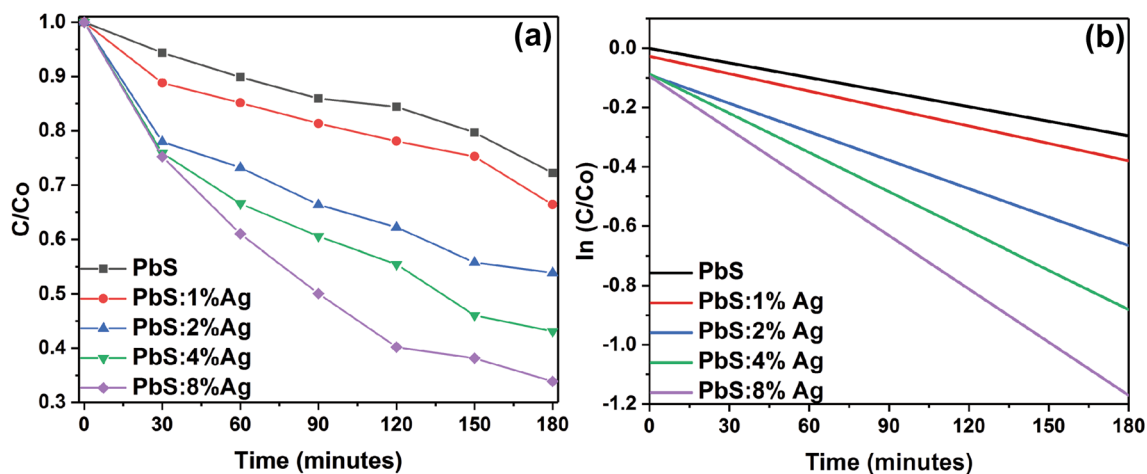

Fig. 7 **a** Variation of the Methylene Blue degradation as a function of time and **b** Evolution of photodegradation kinetic for PbS, P1A, P2A, P4A and P8A samples
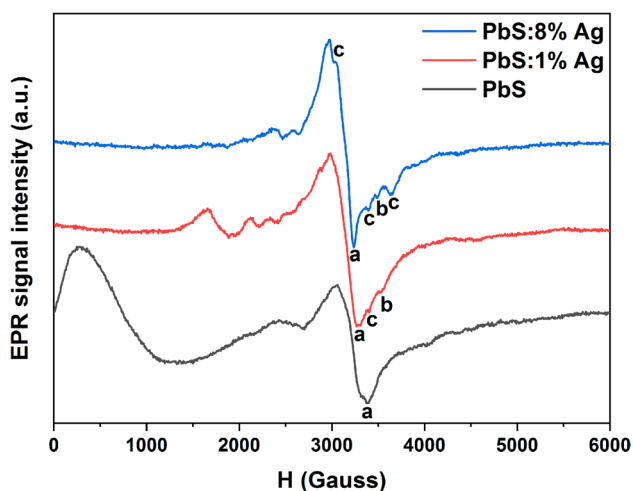
Fig. 8 Room temperature EPR spectra of the PbS, P1A and P8A samples

presence of Ag^0 indicates that some Ag^+ ions adsorbed on the surface of PbS, where they were subsequently reduced, as reported by Scaini et al. [47]. The bands c refer to the Ag^{2+} paramagnetic centers ($4d^9$). The simultaneous appearance of Ag^0 and Ag^{2+} confirm that Ag^+ ions have replaced the Pb^{2+} ions in the PbS lattice, where both are required for system neutrality [48]. In addition, Ag^+ ions have a smaller size than Pb^{2+}, 0.126 and 1.33 nm, respectively. Thus, silver also occupies interstitial sites, generating internal stresses in the lattice [49]. The different sizes and ionic rays between silver and lead promote the generation of oxygen vacancies and, consequently, act as centers that prevent recombination of the e^-/h^+ pairs, generating more reactive oxygen species to act on the photocatalysis [44, 50].

The antimicrobial activity of pure and silver-doped PbS samples was evaluated against *E. coli* and *S. aureus* bacteria and *C. albicans* yeast by measuring the inhibition halos formed. Tests were performed in triplicate and the mean value was used. Figure 9 shows the inhibition halos formed against *S. aureus* (Fig. 9a), *E. coli* (Fig. 9b) and *C. albicans* (Fig. 9c). Table 4 shows the mean values of inhibition halos

Fig. 9 Antimicrobial activity of PbS:xAg (x = 0, 1, 2, 4 and 8 mol%) against **a** *S. aureus*, **b** *E. coli* and **c** *C. albicans*
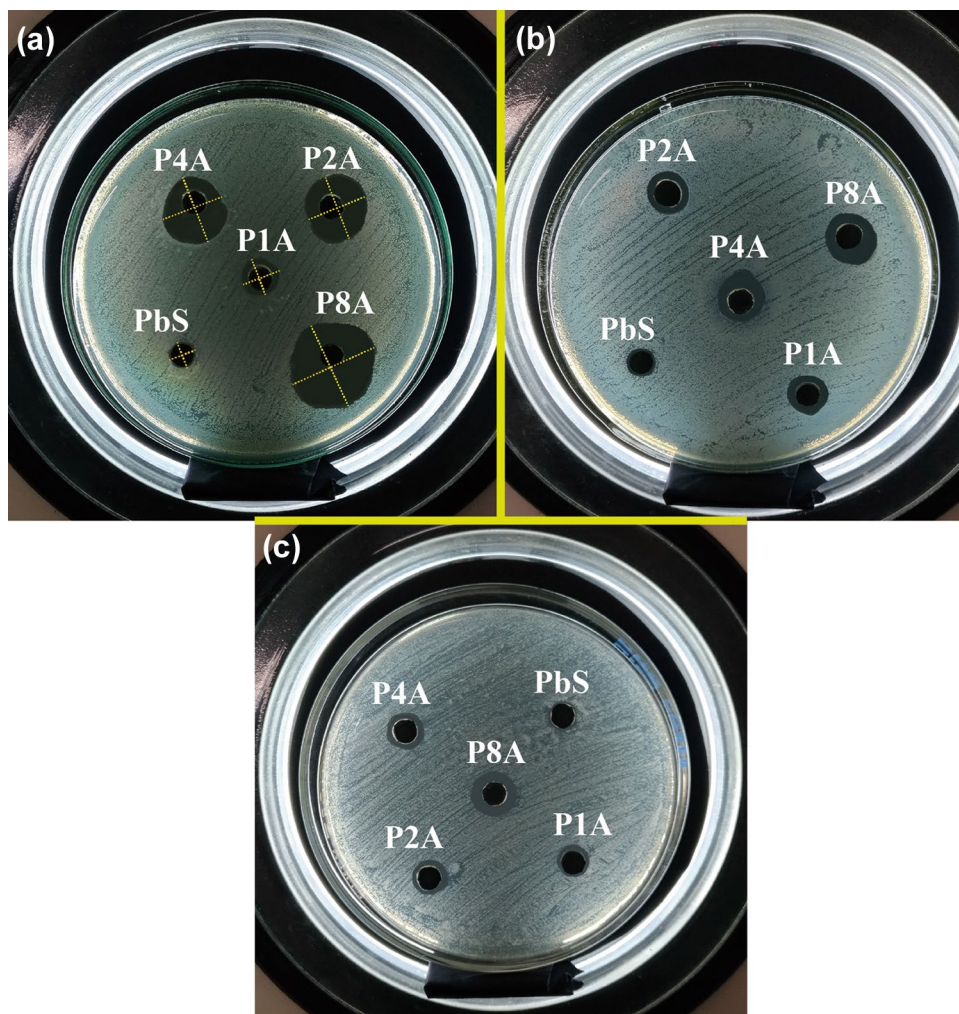
Table 4 Mean values and standard deviation of inhibition halos obtained for pure and silver-doped PbS powders

Sample	Diameter of the inhibition halos (mm)		
	S. aureus	*E. coli*	*C. albicans*
PbS	7.05 ± (0.22)	7.56 ± (0.34)	7.98 ± (0.12)
P1A	9.79 ± (0.18)	10.59 ± (0.39)	8.68 ± (0.15)
P2A	17.15 ± (0.96)	11.25 ± (0.28)	9.30 ± (0.32)
P4A	17.57 ± (0.77)	12.71 ± (0.29)	9.89 ± (0.44)
P8A	22.52 ± (0.55)	13.68 ± (0.58)	12.34 ± (0.17)

act favoring photocatalytic and antimicrobial activities. P8A sample showed more than twice the photocatalytic efficiency in reducing the methylene blue dye concentration compared to PbS. The antimicrobial analysis showed that silver-doped PbS is efficient against *S. aureus* (gram positive) and *E. coli* bacteria (gram negative) and *C. albicans* yeast.

formed as well as the standard deviation. Figure 9a shows the way of obtaining the diameters of inhibition halos.

By means of values obtained for the inhibition halos, it was observed that the substitution of Pb^{2+} cations by Ag^+ favors the antimicrobial activity against *S. aureus, E. and C. albicans*. As shown in Fig. 4, the increase in silver concentration leads to loss of the rectangular morphology of PbS and favors the appearance of smaller particles of irregular morphology, increasing the surface area available to contact the tested microbes. Zare et al. [51] varied the particle size of ZnO through different surfactants and showed that smaller particles present better antimicrobial activities against *E. coli* and *S. aureus* bacteria because they have more active sites for generation of reactive oxygen species (ROS).

In addition, the substitution of Pb^{2+} cations by Ag^+ leads to defects in the crystal structure of PbS, which act to prevent the recombination of generated e^-/h^+ pairs in contact with microbes, providing more ROS in contact with bacteria [52, 53]. The main mechanism of action of metallic nanoparticles is still unknown; however, the literature reports that direct or electrostatic interaction between nanoparticles and the cell surface, the production of reactive oxygen species (ROS) and the cellular internalization of ZnO nanoparticles are the main mechanisms [54–56]. ROS and metal ions act by deforming the cytoplasmic membrane of bacteria, leading to the leakage of intracellular substances and, consequently, the death of bacteria [57, 58].

4 Conclusion

The sonochemical method is efficient to obtain pure and silver-doped PbS powders without the necessity of several steps. XRD patterns show that increasing the amount of silver generates deformations in the crystal lattice of PbS and provides smaller crystallite size. Silver doping also leads to a reduction in particle size and loss of the cubic aspect of PbS. The defects resulting from the addition of silver generate a decrease in the Egap values of the material and act as sites that prevent the recombination of electron/hole pairs, increasing the generation of oxidizing radicals that

References

1. D. Sánchez-Rodríguez, M.G. Méndez Medrano, H. Remita, V. Escobar-Barrios, Photocatalytic properties of BiOCl-TiO2 composites for phenol photodegradation. J. Environ. Chem. Eng. **6**, 1601–1612 (2018)
2. M.B. Askari, Z. Tavakoli Banizi, M. Seifi, S. Bagheri Dehaghi, P. Veisi, Synthesis of TiO2 nanoparticles and decorated multi-wall carbon nanotube (MWCNT) with anatase TiO2 nanoparticles and study of optical properties and structural characterization of TiO2/MWCNT nanocomposite. Optik **149**, 447–454 (2017)
3. A. Kunz, P. Peralta-Zamora, S.G.d. Moraes, N. Durán, Novas tendências no tratamento de efluentes têxteis. Química Nova **25**, 78–82 (2002)
4. T. Stephenson, Wastewater microbiology. By Gabriel Bitton, Wiley–Liss, New York, 1994, ix + 478 pp., price £103.00. ISBN 0 471 30985 0. J. Chem. Technol. Biotechnol. **64**, 213–214 (1995)
5. R.M. Dallago, A. Smaniotto, L.C.A.d. Oliveira, Resíduos sólidos de curtumes como adsorventes para a remoção de corantes em meio aquoso. Química Nova **28**, 433–437 (2005)
6. N.M. Mahmoodi, S. Keshavarzi, M. Ghezelbash, Synthesis of nanoparticle and modelling of its photocatalytic dye degradation ability from colored wastewater. J. Environ. Chem. Eng. **5**, 3684–3689 (2017)
7. X. Rong, F. Qiu, C. Zhang, L. Fu, Y. Wang, D. Yang, Preparation, characterization and photocatalytic application of TiO2–graphene photocatalyst under visible light irradiation. Ceram. Int. **41**, 2502–2511 (2015)
8. C.A. Demarchi, A. Bella Cruz, A. Ślawska-Waniewska, N. Nedelko, P. Dłużewski, A. Kaleta, J. Trzciński, J.D. Magro, J. Scapinello, C.A. Rodrigues, Synthesis of Ag@Fe2O3 nanocomposite based on O-carboxymethylchitosan with antimicrobial activity. Int. J. Biol. Macromol. **107**, 42–51 (2018)
9. J.R. Koduru, S.K. Kailasa, J.R. Bhamore, K.-H. Kim, T. Dutta, K. Vellingiri, Phytochemical-assisted synthetic approaches for silver nanoparticles antimicrobial applications: a review. Adv. Coll. Interface. Sci. **256**, 326–339 (2018)
10. X. Wang, C. Zhou, W. Wang, B. Du, J. Cai, G. Feng, R. Zhang, CdSe nanoparticle-sensitized ZnO sheets for enhanced photocatalytic hydrogen evolution rates. J. Alloy. Compd. **747**, 826–833 (2018)
11. H. Naz, R.N. Ali, X. Zhu, B. Xiang, Effect of Mo and Ti doping concentration on the structural and optical properties of ZnS nanoparticles. Phys. E **100**, 1–6 (2018)
12. X.F. Jia, Q.Y. Hou, Z.C. Xu, L.F. Qu, Effect of Ce doping on the magnetic and optical properties of ZnO by the first principle. J. Magn. Magn. Mater. **465**, 128–135 (2018)
13. A.J. Haider, R.H. Al–, G.R. Anbari, C.T. Kadhim, Salame, Exploring potential environmental applications of TiO2 nanoparticles. Energy Procedia **119**, 332–345 (2017)

14. N.F.A. Neto, L.M.P. Garcia, E. Longo, M.S. Li, C.A. Paskocimas, M.R.D. Bomio, F.V. Motta, Photoluminescence and photocatalytic properties of Ag/AgCl synthesized by sonochemistry: statistical experimental design. J. Mater. Sci. **28**, 12273–12281 (2017)

15. C.-H. Lin, W.-C. Chang, X. Qi, Growth and characterization of pure and doped SnO_2 Films for H_2 gas detection. Proc. Eng. **36**, 476–481 (2012)

16. J.-S. Kim, B.-H. Kang, H.-M. Jeong, S.-W. Kim, B. Xu, S.-W. Kang, Quantum dot light emitting diodes using size-controlled ZnO NPs. Curr. Appl. Phys. **18**, 681–685 (2018)

17. H. Sivaram, D. Selvakumar, A. Alsalme, A. Alswieleh, R. Jayavel, Enhanced performance of PbO nanoparticles and PbO-CdO and PbO-ZnO nanocomposites for supercapacitor application. J. Alloy. Compd. **731**, 55–63 (2018)

18. F.-Y. Liu, J.-H. Lin, Y.-M. Dai, L.-W. Chen, S.-T. Huang, T.-W. Yeh, J.-L. Chang, C.-C. Chen, Preparation of perovskites PbBiO2I/PbO exhibiting visible-light photocatalytic activity. Catal. Today (2018). https://doi.org/10.1016/j.cattod.2018.02.006

19. H. Wang, Y. Li, Y. Wang, J. Ma, S. Hu, H. Hou, J. Yang, Three-dimensional B-doped porous carbon framework anchored with ultrasmall PbO/Pb nanocrystals for lithium storage. Ceram. Int. **43**, 12442–12451 (2017)

20. Z. He, M.D. Hayat, S. Huang, X. Wang, P. Cao, PbO2 electrodes prepared by pulse reverse electrodeposition and their application in benzoic acid degradation. J. Electroanal. Chem. **812**, 74–81 (2018)

21. A.R. Mandal, A. Bekturganova, A. Ishteev, S.P. Choudhury, G. Karunakaran, D. Kunetsov, Effect of silver doping on the current–voltage characteristic of PbS nanorods. Phys. E **79**, 147–151 (2016)

22. Y.-X. Zhang, Z. Ma, Z.-H. Ge, P. Qin, F. Zheng, J. Feng, Highly enhanced thermoelectric properties of Cu1.8S by introducing PbS. J. Alloy. Compd. **764**, 738–744 (2018)

23. H. Guan, Y. Liu, Z. Bai, J. Zhang, S. Yuan, B. Zhang, Ag nanoparticles embedded in N-doped carbon nanofibers: a superior electrocatalyst for hydrogen peroxide detection. Mater. Chem. Phys. **213**, 335–342 (2018)

24. L. Hu, Z. Zhang, R.J. Patterson, Y. Hu, W. Chen, C. Chen, D. Li, C. Hu, C. Ge, Z. Chen, L. Yuan, C. Yan, N. Song, Z.L. Teh, G.J. Conibeer, J. Tang, S. Huang, Achieving high-performance PbS quantum dot solar cells by improving hole extraction through Ag doping. Nano Energy **46**, 212–219 (2018)

25. B. Toby, EXPGUI, a graphical user interface for GSAS. J. Appl. Crystallogr. **34**, 210–213 (2001)

26. D.L. Wood, J. Tauc, Weak absorption tails in amorphous semiconductors. Phys. Rev. B **5**, 3144–3151 (1972)

27. E. Araújo, A.S. Pimenta, F.M.C. Feijó, R.V.O. Castro, M. Fasciotti, T.V.C. Monteiro, K.M.G. Lima, Antibacterial and antifungal activities of pyroligneous acid from wood of Eucalyptus urograndis and Mimosa tenuiflora. J. Appl. Microbiol. **124**, 85–96 (2017)

28. Z. Tshemese, M.D. Khan, S. Mlowe, N. Revaprasadu, Synthesis and characterization of PbS nanoparticles in an ionic liquid using single and dual source precursors. Mater. Sci. Eng. **227**, 116–121 (2018)

29. M. El-Kemary, I. El-Mehasseb, H. El-Shamy, Ag-doped CdO nanocatalysts: preparation, characterization and catechol oxidase activity. J. Mol. Struct. **1161**, 83–88 (2018)

30. H. Rietveld, A profile refinement method for nuclear and magnetic structures. J. Appl. Crystallogr. **2**, 65–71 (1969)

31. M.J. McKelvy, R. Sharma, A.V.G. Chizmeshya, R.W. Carpenter, K. Streib, Magnesium hydroxide dehydroxylation: in situ nanoscale observations of lamellar nucleation and growth. Chem. Mater. **13**, 921–926 (2001)

32. F.V. Motta, A.P.A. Marques, M.S. Li, M.F.C. Abreu, C.A. Paskocimas, M.R.D. Bomio, R.P. Souza, J.A. Varela, E. Longo, Preparation and photoluminescence characteristics of In(OH)3:xTb3 + obtained by Microwave-Assisted Hydrothermal method. J. Alloy. Compd. **553**, 338–342 (2013)

33. R. Kroon, Nanoscience and the Scherrer equation versus the'Scherrer-Gottingen equation'. S. Afr. J. Sci. **109**, 01–02 (2013)

34. S. Hu, R. Ouyang, W.-X. Li, First-principles kinetics study of carbon monoxide promoted Ostwald ripening of Au particles on FeO/Pt(111). J. Energy Chem. (2018). doi:https://doi.org/10.1016/j.jechem.2018.03.023

35. J. Santos, N. Calero, L.A. Trujillo-Cayado, M.C. Garcia, J. Muñoz, Assessing differences between Ostwald ripening and coalescence by rheology, laser diffraction and multiple light scattering. Coll. Surf. B **159**, 405–411 (2017)

36. A. Seweryn, Interactions between surfactants and the skin – Theory and practice. Adv. Coll. Interface. Sci. **256**, 242–255 (2018)

37. C. Dong, X. Xiao, G. Chen, H. Guan, Y. Wang, Morphology control of porous CuO by surfactant using combustion method. Appl. Surf. Sci. **349**, 844–848 (2015)

38. L. Tolvaj, K. Mitsui, D. Varga, Validity limits of Kubelka–Munk theory for DRIFT spectra of photodegraded solid wood. Wood Sci. Technol. **45**, 135–146 (2011)

39. M. Molaei, S. Abbasi, M. Karimipour, F. Dehghan, A simple UV-assisted, room temperature approach for synthesis of water soluble PbS and PbS/CdS core-shell QDs. Mater. Chem. Phys. **216**, 186–190 (2018)

40. E. Akbay, T.G. Ölmez, Sonochemical synthesis and loading of PbS nanoparticles into mesoporous silica. Mater. Lett. **215**, 263–267 (2018)

41. J.C. Sczancoski, L.S. Cavalcante, N. Marana, R. Oliveira da Silva, R.L. Tranquilin, M. Rincón-Joya, P. Pizani, J. Varela, J. Sambrano, M. Li, E. Longo, J. Andrés, Electronic Structure and optical properties of BaMoO4 powders. Curr. Appl. Phys. 10 (2010) 614–624

42. T. Ali, A. Ahmed, U. Alam, I. Uddin, P. Tripathi, M. Muneer, Enhanced photocatalytic and antibacterial activities of Ag-doped TiO_2 nanoparticles under visible light. Mater. Chem. Phys. **212**, 325–335 (2018)

43. M.M. Momeni, M. Hakimian, A. Kazempour, In-situ manganese doping of TiO_2 nanostructures via single-step electrochemical anodizing of titanium in an electrolyte containing potassium permanganate: a good visible-light photocatalyst. Ceram. Int. **41**, 13692–13701 (2015)

44. M. Mittal, A. Gupta, O.P. Pandey, Role of oxygen vacancies in Ag/Au doped CeO2 nanoparticles for fast photocatalysis. Sol. Energy **165**, 206–216 (2018)

45. M. Stefan, C. Leostean, O. Pana, D. Toloman, A. Popa, I. Perhaita, M. Senilă, O. Marincas, L. Barbu-Tudoran, Magnetic recoverable Fe3O4-TiO_2:Eu composite nanoparticles with enhanced photocatalytic activity. Appl. Surf. Sci. **390**, 248–259 (2016)

46. H. Pan, X. Zhao, Z. Fu, W. Tu, P. Fang, H. Zhang, Visible-light induced photocatalysis of AgCl@Ag/titanate nanotubes/nitrogen-doped reduced graphite oxide composites. Appl. Surf. Sci. **442**, 547–555 (2018)

47. M.J. Scaini, G.M. Bancroft, S.W. Knipe, X.P.S. An, AES, and SEM study of the interactions of gold and silver chloride species with PbS and FeS2: Comparison to natural samples. Geochim. Cosmochim. Acta **61**, 1223–1231 (1997)

48. A.R. Mandal, S.K. Mandal, Electron spin resonance in silver-doped PbS nanorods. J. Exp. Nanosci. **5**, 189–198 (2010)

49. B. Clerjaud, A. Gélineau, Strong spin-lattice coupling of Kramers doublets. Phys. Rev. B **16**, 82–85 (1977)

50. L. Elsellami, F. Dappozze, A. Houas, C. Guillard, Effect of Ag + reduction on the photocatalytic activity of Ag-doped TiO2. Superlattices Microstruct. **109**, 511–518 (2017)

51. M. Zare, K. Namratha, K. Byrappa, D.M. Surendra, S. Yallappa, B. Hungund, Surfactant assisted solvothermal synthesis of ZnO

nanoparticles and study of their antimicrobial and antioxidant properties. J. Mater. Sci. Technol. **34**, 1035–1043 (2018)

52. M. Rehan, T.A. Khattab, A. Barohum, L. Gätjen, R. Wilken, Development of Ag/AgX (X = Cl, I) nanoparticles toward antimicrobial, UV-protected and self-cleanable viscose fibers. Carbohyd. Polym. **197**, 227–236 (2018)

53. D. Rehana, D. Mahendiran, R. Manigandan, V. Narayanan, A. Kalilur, Rahiman, Evaluation of photocatalytic, antimicrobial and anticancer activities of ZnO/MS (M = Zn, Cd or Pb) core/shell nanoparticles. Mater. Sci. Eng. **225**, 20–32 (2017)

54. A.V. Badarinath, K. Mallikarjuna Rao, C. Madhu Sudhana Chetty, S. Ramkanth, T.V.S. Rajan, K. Gnanaprakash, A review on In-vitro antioxidant methods: comparisions, correlations and considerations. Int. J. PharmTech Res. **2**, 1276–1285 (2010)

55. S.M. Dizaj, F. Lotfipour, M. Barzegar-Jalali, M.H. Zarrintan, K. Adibkia, Antimicrobial activity of the metals and metal oxide nanoparticles. Mater. Sci. Eng. **44**, 278–284 (2014)

56. Y. Xie, Y. He, P.L. Irwin, T. Jin, X. Shi, Antibacterial activity and mechanism of action of zinc oxide nanoparticles against Campylobacter jejuni. Appl. Environ. Microbiol. **77**, 2325–2331 (2011)

57. M. Li, L. Zhu, D. Lin, Toxicity of ZnO nanoparticles to escherichia coli: mechanism and the influence of medium components. Environ. Sci. Technol. **45**, 1977–1983 (2011)

58. N.M. Franklin, N.J. Rogers, S.C. Apte, G.E. Batley, G.E. Gadd, P.S. Casey, Comparative toxicity of nanoparticulate ZnO, Bulk ZnO, and ZnCl$_2$ to a freshwater microalga (*Pseudokirchneriella subcapitata*): the importance of particle solubility. Environ. Sci. Technol. **41**, 8484–8490 (2007)